Supporting Information

Decoupling the Roles of Carbon and Metal Oxides on the Electrocatalytic Reduction of Oxygen on La$_{1-x}$Sr$_x$CoO$_{3-\delta}$ Perovskite Composite Electrodes

J. Tyler Mefford,[a,b,] Aleksandr Kurilovich,[c] Jennette Saunders,[a] William G. Hardin,[b,d,§] Artem M. Abakumov,[c,e] Robin P. Forslund,[a,b] Antoine Bonnefont,[f] Sheng Dai,[g] Keith P. Johnston,[d,h] Keith J. Stevenson[c,†]*

[a]Department of Chemistry, [b]Center for Nano and Molecular Science and Technology,[d] Texas Materials Institute, [h]Department of Chemical Engineering, The University of Texas at Austin, Austin, Texas 78712, USA. [c]Center for Electrochemical Energy Storage CREI, Skolkovo Institute of Science and Technology, 143025 Moscow, Russia. [e]Electron Microscopy for Materials Sciences EMAT, University of Antwerp, B-2020 Antwerp, Belgium. [f]Institut de Chimie de Strasbourg, University of Strasbourg, 67070 Strasbourg, France. [g]Chemical Sciences Division, Oak Ridge National Laboratory, Oak Ridge, TN 37831, USA.

[†]**Corresponding Author:** k.stevenson@skoltech.ru
[*]**Current Address:** Department of Material Science and Engineering, Stanford University, 496 Lomita Mall, Stanford, CA 94305, USA
[§]**Current Address:** Exponent Failure Analysis Associates, Natick, MA 01760, USA

Surface Oxygen Chemistry:

To probe the chemical nature of oxygen species in the catalysts surface, core-level O 1s high-resolution X-ray photoelectron spectroscopy (XPS) was performed on the LSCO samples. The collected spectra were deconvoluted using a method derived from Mickevicius and Stoerzinger, yet modified to account for surface carbon contamination and the presence of Sr.[1,2] The spectra, shown in Figure 5.1 contain eight types of oxygen species: hydroxylated surface oxygen bound to Co or La (Surface OH: 531.3 $\pm$ 0.3 eV);[2–4]hydroxylated surface oxygen bound to Sr (Sr-OH: 530.5 $\pm$ 0.3 eV);[5,6]surface oxide bound to La (La-O: 528.8 $\pm$ 0.2 eV),[1,4,7]Co (Co-O: 529.8 $\pm$ 0.1 eV),[3,5,7]or Sr (Sr-O: Sr-OH minus 2.3 eV);[5,6]adsorbed water (H_2O: 534.5 $\pm$ 0.65 eV),[2,5,8]ether (C-O-C: 533.15 $\pm$ 0.15), and carbonate combined with carbonyl functionality (CO_3 & C=O: 531.6 $\pm$ 0.2 eV;).[2,3,6,8] Distinguishing between the species of lattice oxygen in the catalyst surface, it was found that the degree of surface hydroxylation could be correlated to the Sr content as well as to the vacancy concentration, with $SrCoO_{2.7}$ having ~63 relative atomic % hydroxylated surface oxygen compared to $LaCoO_{3.005}$ with ~7 rel. at. % hydroxylated surface oxygen. These results are shown in Figure 5.1, where the increase of the majority of protonated surface oxygen could be associated predominantly with Sr-OH type species. It is hypothesized that the degree of hydroxylation are a result of the surface vacancies acting as dissociation sites for water due to their Lewis acidity, whereby a proton is transferred to a lattice oxide species and the remaining hydroxide ion fills the surface vacancy and in doing so donates its electron pair to the Lewis acid vacancy site.[9–11] This proton transfer and subsequent filling of a surface vacancy should be thermodynamically favorable due to Pauling's electrostatic valence rules in which the surface of an ionic crystal is stabilized to a greater degree by coverage with univalent ions rather than multivalent ions, and is expected to occur in all high oxygen vacancy materials.[12]

N$_2$ sorption surface area measurement of Vulcan carbon XC-72:

BET surface area measurements were performed through nitrogen sorption on a Quantachrome

Instruments NOVA 2000 high-speed surface area BET analyzer at a temperature of 77K.

Scanning Electron Microscopy of LSCO/Carbon Composites:

Samples were prepared by dispersing unsupported material in ethanol at 0.1 mg mL^{-1} or

supported material at 0.2 mg mL^{-1} and dropcasting onto silicon wafers which were then dried at

85°C for 30 minutes. Images were taken on a Hitachi S5500 SEM using an accelerating voltage

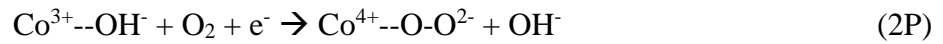of 30 kV and a probe current of 15 mA.

Microkinetic modeling details:

The suggested ORR mechanisms for perovskites consist of 5 reaction steps:

1) Surface Co^{4+}/Co^{3+} redox transition.

$$Co^{4+}\text{--}O^{2-} + H_2O + e^- \rightarrow Co^{3+}\text{--}OH^- + OH^- \hspace{2cm} (1P)$$
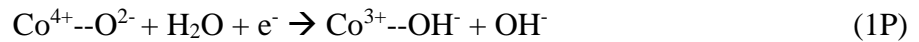
2) Oxygen adsorption/ desorption on/from the Co^{3+} active sites, combined with the first electron transfer step.

$$Co^{3+}\text{--}OH^- + O_2 + e^- \rightarrow Co^{4+}\text{--}O\text{-}O^{2-} + OH^- \hspace{2cm} (2P)$$

3) The reduction of the adsorbed oxygen into the HO_2^- / oxidation of HO_2^- to the oxygen.

$$Co^{4+}\text{--}O\text{-}O^{2-} + H_2O + e^- \rightarrow Co^{3+}\text{--}O\text{-}OH^- + OH^- \hspace{2cm} (3P)$$
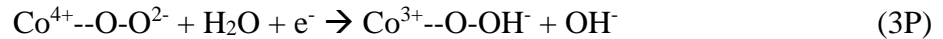
4) Chemical decomposition of the adsorbed HO_2^-. (reaction mechanism with 4PC step)

$$Co^{3+}\text{--}O\text{-}OH^- + Co^{3+}\text{--}OH^- \rightarrow 2Co^{4+}\text{--}O^{2-} + H_2O \hspace{2cm} (4PC)$$
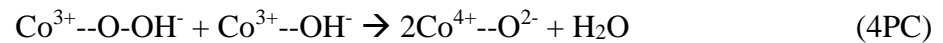
Electrochemical reduction of HO_2^- to OH^- / oxidation of OH- to HO_2^-. (reaction mechanism with

4PE step)

$$Co^{3+}\text{--}O\text{-}OH^- + e^- \rightarrow Co^{4+}\text{--}O^{2-} + OH^- \hspace{2cm} (4PE)$$

5) The adsorption/desorption of HO_2^- on/from the Co^{3+} surface site.

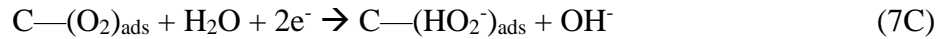$$Co^{3+}\text{--}OH^- + HO_2^- \rightarrow Co^{3+}\text{--}O\text{-}OH^- + OH^- \hspace{2cm} (5P)$$
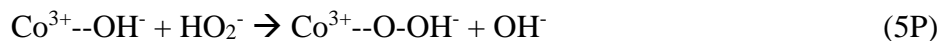
The ORR and HPRR/HPOR reactions on VC and NC carbons were simulated using the following effective mechanism:

6) Oxygen adsorption/ desorption on/from the carbon active sites

$$C + O_2 \rightarrow C\text{—}(O_2)_{ads} \tag{6C}$$

7) The reduction of the adsorbed oxygen into the HO_2^-/oxidation of adsorbed oxygen into the HO_2^-

$$C\text{—}(O_2)_{ads} + H_2O + 2e^- \rightarrow C\text{—}(HO_2^-)_{ads} + OH^- \tag{7C}$$

8) HO_2^- adsorption/desorption on/from the carbon active site.

$$C\text{—}(HO_2^-)_{ads} \rightarrow C + HO_2^- \tag{8C}$$

9) Effective reaction step for the oxygen spillover between the N-doped active sites and Co^{3+} cations (also modeled on VC for consistency)

$$C\text{—}(O_2)_{ads} + Co^{3+}\text{--}OH + e^- \rightarrow C + Co^{4+}\text{--}O\text{-}O + OH^- \tag{9}$$
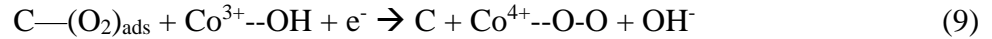
10) Effective reaction step for the HO_2^- spillover between the N-doped active sites and Co^{3+} cations

$$C\text{—}(HO_2^-)_{ads} + Co^{3+}\text{--}OH \rightarrow C + Co^{3+}\text{--}O\text{-}OH + OH^- \tag{10}$$
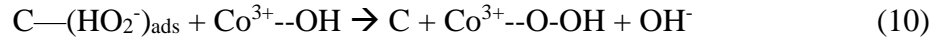
The electrode surface is considered to be flat with the perfectly intermixed carbon and perovskite active sites which are equally accessible by the O_2 and HO_2^- species, so the O_2 and HO_2^- concentration is considered the same in the vicinity of perovskite and carbon active sites. The diffusion profile was assumed to be linear for the O_2 and HO_2^- species in the solution. The diffusion in the bulk of the electrode was neglected because of the low experimental catalyst loading. Diffusivities of O_2 and HO_2^-, kinematic viscosity, and oxygen solubility were taken from the literature data.[13] LCO and VC surface active sites densities were obtained by renormalization of the estimates for LCO and Sibunit-152 carbon from works by BET surface areas and loadings ratios for the materials synthesized in this and abovementioned works.[14,15]

Forward and backward rate constants ratio of steps 1) (6C), (7C), (8C); 2) (2P), (3P), (5P); 3) (2P), (3P), (5P), (9); 4) (2P), (3P), (5P), (10) were simultaneously adjusted and fixed in order to reproduce pH-corrected equilibrium potential $E_{HO2-/O2}$ =0.74 V vs. RHE at pH = 13. The same procedure was applied to adjust the rate constants ratio for the steps (4PE), (4PC) to reproduce the pH corrected equilibrium potential $E_{HO2-/OH-}$ = 1.74 vs. RHE at pH = 13. It was consistently obtained that the (4PE) and (4PC) steps are irreversible at the potential range at which the ORR and HPRR/HPOR experiments were carried out.

$$v_{1P} = k_1 \theta_{O_P} \exp\left(-\frac{\alpha_1 F(E-E_1^0)}{RT}\right) - k_{-1}\left(1 - \theta_{O_P} - \theta_{O_{2,P}} - \theta_{HO_{2,P}}\right) \exp\left(\frac{(1-\alpha_1)F(E-E_1^0)}{RT}\right) \quad (S1)$$

$$v_{2P} = k_2 c_{O_2}\left(1 - \theta_{O_P} - \theta_{O_{2,P}} - \theta_{HO_{2,P}}\right) \exp\left(-\frac{\alpha_2 FE}{RT}\right) - k_{-2}\theta_{O_{2,P}} \exp\left(\frac{(1-\alpha_2)FE}{RT}\right) \quad (S2)$$

$$v_{3P} = k_3 \theta_{O_{2,P}} \exp\left(-\frac{\alpha_3 FE}{RT}\right) - k_{-3}\theta_{HO_{2,P}} \exp\left(\frac{(1-\alpha_3)FE}{RT}\right) \quad (S3)$$

$$v_{4PC} = k_4\left(1 - \theta_{O_P} - \theta_{O_{2,P}} - \theta_{HO_{2,P}}\right)\theta_{HO_{2,P}} - k_{-4}\theta_{O_P}^2 \quad (S4)$$

$$v_{4PE} = k_4 \theta_{HO_{2,P}} \exp\left(-\frac{\alpha_4 FE}{RT}\right) - k_{-4}\theta_{O_P} \exp\left(\frac{(1-\alpha_4)FE}{RT}\right) \quad (S5)$$

$$v_{5P} = k_5 c_{HO_2^-}\left(1 - \theta_{O_P} - \theta_{O_{2,P}} - \theta_{HO_{2,P}}\right) - k_{-5}\theta_{HO_{2,P}} \quad (S6)$$

$$v_{6C,N} = k_{6C,N} c_{O_2}\left(1 - \theta_{O_{2C,N}} - \theta_{HO_{2C,N}^-}\right) - k_{-6C,N}\theta_{O_{2C,N}} \quad (S7)$$

$$v_{7C,N} = k_{7C,N} \theta_{O_{2C,N}} \exp\left(-\frac{\alpha_7 FE}{RT}\right) - k_{-7C,N}\theta_{HO_{2C,N}^-} \exp\left(\frac{(1-\alpha_7)FE}{RT}\right) \quad (S8)$$

$$v_{8C,N} = k_{8C,N} \theta_{HO_{2C,N}^-} - k_{-8C,N} c_{HO_{2C,N}^-}\left(1 - \theta_{O_{2C,N}} - \theta_{HO_{2C,N}^-}\right) \quad (S9)$$

$$v_{9N} = k_9 \theta_{O_{2N}}\left(1 - \theta_{O_P} - \theta_{O_{2,P}} - \theta_{HO_{2,P}}\right) \exp\left(-\frac{\alpha_9 FE}{RT}\right) - k_{-9}\left(1 - \theta_{O_{2C,N}} - \theta_{HO_{2C,N}^-}\right) \exp\left(\frac{(1-\alpha_9)FE}{RT}\right) \quad (S10)$$

$$v_{10N} = k_{10} \theta_{HO_{2N}^-}\left(1 - \theta_{O_P} - \theta_{O_{2,P}} - \theta_{HO_{2,P}}\right) - k_{-10}\theta_{HO_{2,P}}\left(1 - \theta_{O_{2N}} - \theta_{HO_{2N}^-}\right) \quad (S11)$$

The ORR current potential curves were simulated under the stationary conditions:

$$\frac{d\theta_{O2,N}}{dt} = 0 = v_{6N} - v_{7N} - \frac{\Gamma_P}{\Gamma_N} v_{9N} \tag{S12}$$

$$\frac{d\theta_{O2,C}}{dt} = 0 = v_{6C} - v_{7C} \tag{S13}$$

$$\frac{d\theta_{HO_2^-,N}}{dt} = 0 = v_{7N} - v_{8N} - \frac{\Gamma_P}{\Gamma_N} v_{10N} \tag{S14}$$

$$\frac{d\theta_{HO_2^-,C}}{dt} = 0 = v_{7C} - v_{8C} \tag{S15}$$

When the pathway follows (4PC):
$$\frac{d\theta_{O,P}}{dt} = 0 = 2v_{4PC} - v_{1P} \tag{S16}$$

When the pathway follows (4PE):
$$\frac{d\theta_{O,P}}{dt} = 0 = v_{4PE} - v_{1P} \tag{S17}$$

$$\frac{d\theta_{O2,P}}{dt} = 0 = v_{2P} - v_{3P} + v_{9N} \tag{S18}$$

$$\frac{d\theta_{HO2,P}}{dt} = 0 = v_{3P} - v_{4P} + v_{5P} + v_{10N} \tag{S19}$$

Given the linear concentration profile in the solution, one can write down the mass-balance equations for O_2 and HO_2^-:

$$D_{O_2} \frac{dc_{O_2}}{dx} \approx D_{O_2} \frac{c_{O_2}^{bulk} - c_{O_2}^s}{\delta_{O_2}} = \Gamma_C v_{6C} + \Gamma_N v_{6N} + \Gamma_P v_{2P} \tag{S20}$$

$$D_{HO_2^-} \frac{dc_{HO_2^-}}{dx} \approx D_{HO_2^-} \frac{c_{HO_2^-}^{bulk} - c_{HO_2^-}^s}{\delta_{HO_2^-}} = -\Gamma_C v_{8C} - \Gamma_N v_{8N} + \Gamma_P v_{5P} \tag{S21}$$

Here, D_{O_2}, $D_{HO_2^-}$ are the O_2 and HO_2^- diffusion coefficients, $c_{O_2}^{bulk}$, $c_{HO_2^-}^{bulk}$ are the O_2 and HO_2^- concentrations in the solution bulk, $c_{O_2}^s$, $c_{HO_2^-}^s$ are O_2 and HO_2^- concentrations in the vicinity of the electrode surface, $\delta_{HO_2^-}$, δ_{O_2} are the O_2 and HO_2^- diffusion layer thickness, $\theta_{O_{2C}}$, $\theta_{HO_{2C}^-}$ are the O_2 and HO_2^- surface coverages on carbon active sites, $\theta_{O_{2N}}$, $\theta_{HO_{2N}^-}$ are the O_2 and HO_2^- surface coverages on nitrogen-doped carbon active sites, and $\theta_{O_{2p}}$, $\theta_{HO_{2p}}$, θ_{O_p} are the O_2, HO_2, and O surface coverages on perovskite. The diffusion layer thicknesses are estimated from the analytical solution for the RDE experiment using the electrode rotation rate W and kinematic viscosity υ:[16,17]

$$\delta_{O_2} = 1.61 D_{O_2}^{1/3} w^{-1/2} v^{1/6} \tag{S22}$$

$$\delta_{HO_2^-} = 1.61 D_{HO_2^-}^{1/3} w^{-1/2} v^{1/6} \tag{S23}$$

$\Gamma_C, \Gamma_N, \Gamma_P$ are C, N-doped, and perovskite surface active sites densities for ORR and HPRR/HPOR, which were calculated from the estimations provided in the work using the renormalization by the catalyst loading and BET surface areas.[14]

ORR and HPRR/HPOR were calculated as:

$$I_{ORR,HPRR/HPOR}^{4PC} = -2F\Gamma_{VC}v_{7C} - 2F\Gamma_N v_{7n} - F\Gamma_P(v_{1P} + v_{2P} + v_{3P} + v_9) \tag{S24}$$

$$I_{ORR,HPRR/HPOR}^{4PE} = -2F\Gamma_{VC}v_{7C} - 2F\Gamma_N v_{7n} - F\Gamma_P(v_{1P} + v_{2P} + v_{3P} + v_{4PE} + v_9) \tag{S25}$$

Table S1. Adjusted model parameters.						
Parameter	VC (4PC/4PE)	NC (4PC/4PE)	LCO/VC (4PC/4PE)	LCO/NC (4PC/4PE)	LSCO64/VC (4PC)	LSCO64/NC (4PC)
k_1, s^{-1}	-/-	-/-	$9.6 \times 10^{-1}/5.6 \times 10^{-1}$	$9.6 \times 10^{-1}/5.6 \times 10^{-1}$	9.6×10^{-1}	9.6×10^{-1}
k_{-1}, s^{-1}	-/-	-/-	$9.6 \times 10^{-1}/5.6 \times 10^{-1}$	$9.6 \times 10^{-1}/5.6 \times 10^{-1}$	9.6×10^{-1}	9.6×10^{-1}
k_2, cm^3 mol^{-1} s^{-1}	-/-	-/-	$1.3 \times 10^{10}/1.6 \times 10^{11}$	$1.3 \times 10^{10}/1.6 \times 10^{11}$	1.0×10^{16}	1×10^{16}
k_{-2}, s^{-1}	-/-	-/-	$2.8 \times 10^{-9}/3.5 \times 10^{-8}$	$2.8 \times 10^{-9}/3.5 \times 10^{-8}$	2.2×10^{-3}	2.3×10^{-3}
k_3, s^{-1}	-/-	-/-	$1.3 \times 10^{10}/2.9 \times 10^{11}$	$1.3 \times 10^{10}/2.9 \times 10^{11}$	1.2×10^{8}	1.2×10^{8}
k_{-3}, s^{-1}	-/-	-/-	$1.4 \times 10^{-6}/3.5 \times 10^{-4}$	$1.4 \times 10^{-6}/3.5 \times 10^{-4}$	1.4×10^{-7}	1.4×10^{-7}
k_4, s^{-1}	-/-	-/-	$2.5 \times 10^{1}/1.4 \times 10^{10}$	$2.5 \times 10^{1}/1.4 \times 10^{10}$	3.0×10^{1}	3.0×10^{1}
k_{-4}, s^{-1}	-/-	-/-	0/0	0/0	0	0
k_5, cm^3 mol^{-1} s^{-1}	-/-	-/-	$4 \times 10^{8}/4 \times 10^{6}$	$4 \times 10^{8}/4 \times 10^{6}$	4×10^{8}	4×10^{8}
k_{-5}, s^{-1}	-/-	-/-	$1 \times 10^{3}/1 \times 10^{1}$	$1 \times 10^{3}/1 \times 10^{1}$	1×10^{3}	1×10^{3}
k_{6C}, cm^3 mol^{-1} s^{-1}	$1.5 \times 10^{8}/1.5 \times 10^{8}$	$1.5 \times 10^{8}/1.5 \times 10^{8}$	$1.5 \times 10^{8}/1.5 \times 10^{8}$	$1.5 \times 10^{8}/1.5 \times 10^{8}$	1.5×10^{8}	1.5×10^{8}
k_{-6C}, cm s^{-1}	$1.6 \times 10^{3}/1.6 \times 10^{3}$	$1.6 \times 10^{3}/1.6 \times 10^{3}$	$1.6 \times 10^{3}/1.6 \times 10^{3}$	$1.6 \times 10^{3}/1.6 \times 10^{3}$	1.6×10^{3}	1.6×10^{3}
k_{7C}, s^{-1}	$5.5 \times 10^{9}/5.5 \times 10^{9}$	$5.5 \times 10^{9}/5.5 \times 10^{9}$	$5.5 \times 10^{9}/5.5 \times 10^{9}$	$5.5 \times 10^{9}/5.5 \times 10^{9}$	5.5×10^{9}	5.5×10^{9}

k_{-7C}, s^{-1}	$1.6 \times 10^{-1}/1.6 \times 10^{-1}$	$1.6 \times 10^{-1}/1.6 \times 10^{-1}$	$1.6 \times 10^{-1}/1.6 \times 10^{-1}$	$1.6 \times 10^{-1}/1.6 \times 10^{-1}$	1.6×10^{-1}	1.6×10^{-1}
k_{8C}, s^{-1}	$1.8 \times 10^{3}/1.8 \times 10^{3}$	$1.8 \times 10^{3}/1.8 \times 10^{3}$	$1.8 \times 10^{3}/1.8 \times 10^{3}$	$1.8 \times 10^{3}/1.8 \times 10^{3}$	1.8×10^{3}	1.8×10^{3}
k_{-8C}, cm^3 mol s^{-1}	$2.0 \times 10^{3}/2.0 \times 10^{3}$	$2.0 \times 10^{3}/2.0 \times 10^{3}$	$2.0 \times 10^{3}/2.0 \times 10^{3}$	$2.0 \times 10^{3}/2.0 \times 10^{3}$	2.0×10^{3}	2.0×10^{3}
k_{6NC}, cm^3 mol^{-1} s^{-1}	-/-	$1.5 \times 10^{8}/1.5 \times 10^{8}$	-/-	$1.5 \times 10^{8}/1.5 \times 10^{8}$	-	1.5×10^{8}
k_{-6N}, cm s^{-1}	-/-	$1.6 \times 10^{3}/1.6 \times 10^{3}$	-/-	$1.6 \times 10^{3}/1.6 \times 10^{3}$	-	1.6×10^{3}
k_{7N}, s^{-1}	-/-	$3.7 \times 10^{8}/3.7 \times 10^{8}$	-/-	$3.7 \times 10^{8}/3.7 \times 10^{8}$	-	3.7×10^{8}
k_{-7N}, s^{-1}	-/-	$6.9 \times 10^{-3}/6.9 \times 10^{-3}$	-/-	$6.9 \times 10^{-3}/6.9 \times 10-3$	-	6.9×10^{-3}
k_{8N}, s^{-1}	-/-	$4.2 \times 10^{3}/4.2 \times 10^{3}$	-/-	$4.2 \times 10^{3}/4.2 \times 10^{3}$	-	4.2×10^{3}
k_{-8N}, cm^3 mol s^{-1}	-/-	$4.6 \times 10^{3}/4.6 \times 10^{3}$	-/-	$4.6 \times 10^{3}/4.6 \times 10^{3}$	-	4.6×10^{3}
k_{9}, s^{-1}	-/-	-/-	$8.8 \times 10^{11}/-$	$1.7 \times 10^{12}/8.8 \times 10^{11}$	-	3.5×10^{12}
k_{-9}, s^{-1}	-/-	-/-	$1.8 \times 10^{-2}/-$	$3.6 \times 10^{-2}/2.3 \times 10^{1}$	-	7.2×10^{-2}
k_{10}, s^{-1}	-/--	-/-	-/-	$1 \times 10^{5}/1 \times 10^{4}$	-	-
k_{-10}, s^{-1}	-/-	-/-	-/-	$2.8 \times 10^{-1}/2.8 \times 10^{-2}$	-	-
E_1^0 V vs. RHE	-/-	-/-	0.933	0.933	1.053	1.053
α_1	-/-	-/-	0.5/0.5	0.5/0.5	0.5	0.5
α_2	-/-	-/-	0.5/0.5	0.5/0.5	0.8	0.8
α_3	-/-	-/-	0.5/0.5	0.5/0.5	0.5	0.5
α_4	-/-	-/-	-/0.5	-/0.5	-	-
α_{7C}	0.8/0.8	0.8/0.8	0.8/0.8	0.8/0.8	0.8	0.8
α_{7NC}	-/-	0.5	-/-	0.5	-	0.5
α_9	-/-	-/-	-/-	0.8/0.8	-	0.8
Γ_C	$1.9 \times 10^{-8}/1.9 \times 10^{-8}$	$1.9 \times 10^{-8}/1.9 \times 10^{-8}$	$1.9 \times 10^{-8}/1.9 \times 10^{-8}$	$1.9 \times 10^{-8}/1.9 \times 10^{-8}$	1.9×10^{-8}	1.9×10^{-8}
Γ_{NC}	-/-	$3.9 \times 10^{-10}/3.9 \times 10^{-10}$	-/-	$3.9 \times 10^{-10}/3.9 \times 10^{-10}$	-	3.9×10^{-10}
Γ_{LSCO}	-/-	-/-	$6.1 \times 10^{-10}/6.1 \times 10^{-10}$	$6.1 \times 10^{-10}/6.1 \times 10^{-10}$	6.1×10^{-10}	6.1×10^{-10}

v, cm^2 s^{-1}	1.0×10^{-2}	1.0×10^{-2}	1.0×10^{-2}	1.0×10^{-2}	1.0×10^{-2}	1.0×10^{-2}
$c_{O2}*$	1.2×10^{-6}	1.2×10^{-6}	1.2×10^{-6}	1.2×10^{-6}	1.2×10^{-6}	1.2×10^{-6}
$c_{HO2-}*$	1.2×10^{-6}	1.2×10^{-6}	1.2×10^{-6}	1.2×10^{-6}	1.2×10^{-6}	1.2×10^{-6}
D_{O2}	1.9×10^{-5}	1.9×10^{-5}	1.9×10^{-5}	1.9×10^{-5}	1.9×10^{-5}	1.9×10^{-5}
D_{HO2-}	0.8×10^{-5}	0.8×10^{-5}	0.8×10^{-5}	0.8×10^{-5}	0.8×10^{-5}	0.8×10^{-5}
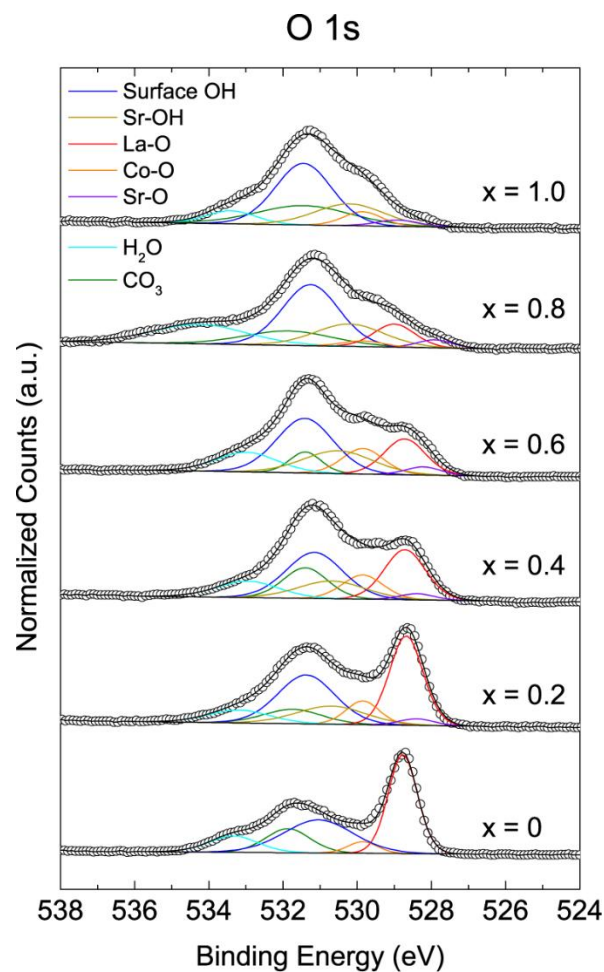
Figure S1: O1s XPS of $La_{1-x}Sr_xCoO_{3-\delta}$. The relative atomic % surface hydroxylation is calculated as ([Surface OH] + [Sr-OH])/([Surface OH] + [Sr-OH] + [La-O] + [Sr-O] + [Co-O]). The LSCO series shows an increase in the relative amount of surface hydroxide type oxygen in the crystals concomitant with the increase of Sr.
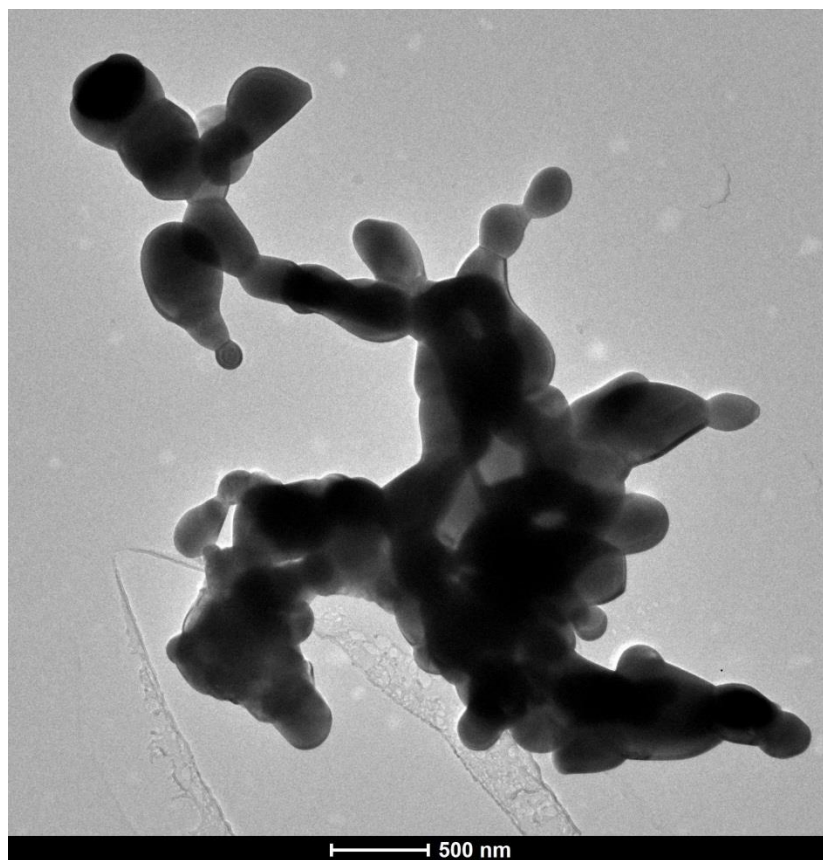
Figure S2: Bright field TEM image of the LaCoO$_3$ nanoparticles.
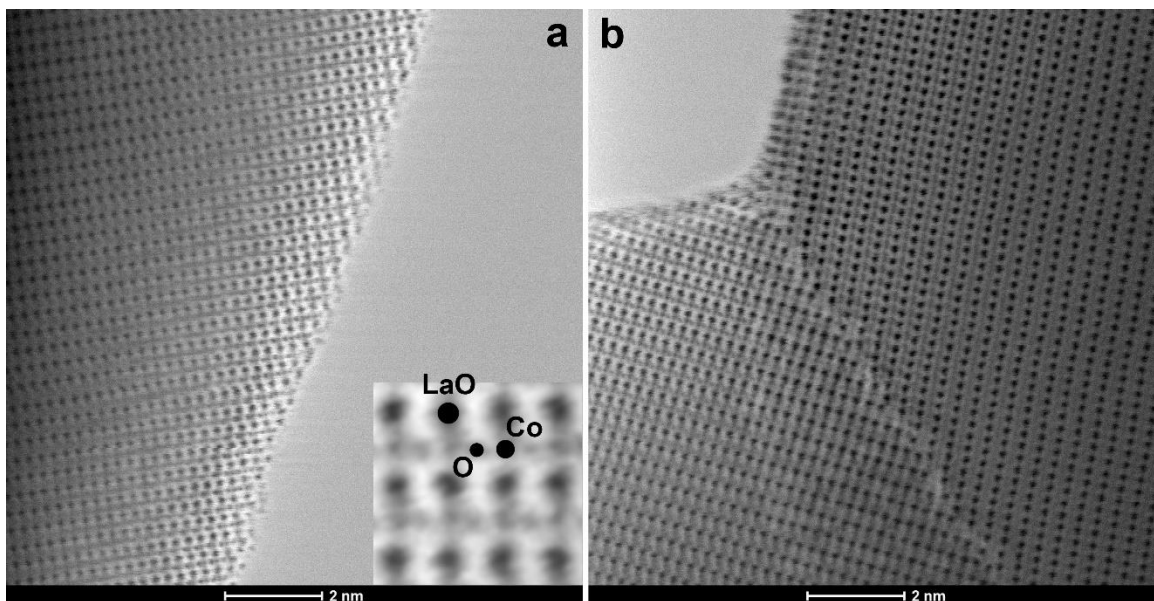
Figure S3: (a) $<1\bar{1}0>_p$ annular bright field (ABF) STEM image of the irregularly structured curved surface with numerous sub-nm sized steps. Such surface may arise from cleaving along the incoherent grain boundaries between the nanocrystals shown in **(b)**. Note that in contrast to the HAADF-STEM images the atomic columns in the ABF-STEM images appear dark on bright background. The insert shows enlarged part of the image with atomic columns assigned.
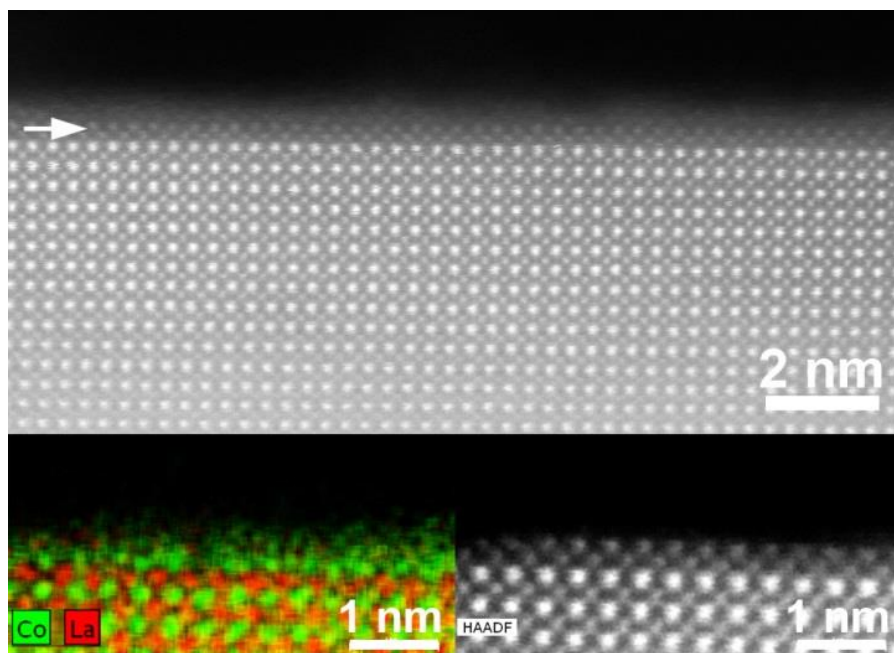
Figure S4: HAADF-STEM image and atomic resolution EDX compositional Co (green) and La (red) map of the surface layer of the $\{100\}_p$ facet in the $<001>_p$ orientation. The last layer of the perovskite structure is (CoO_2). The extra surface layer (marked with an arrow) contains mostly Co and together with the (CoO_2) layer forms the staggered arrangement of the Co columns. Note that no conclusion of the O distribution can be made from these data.
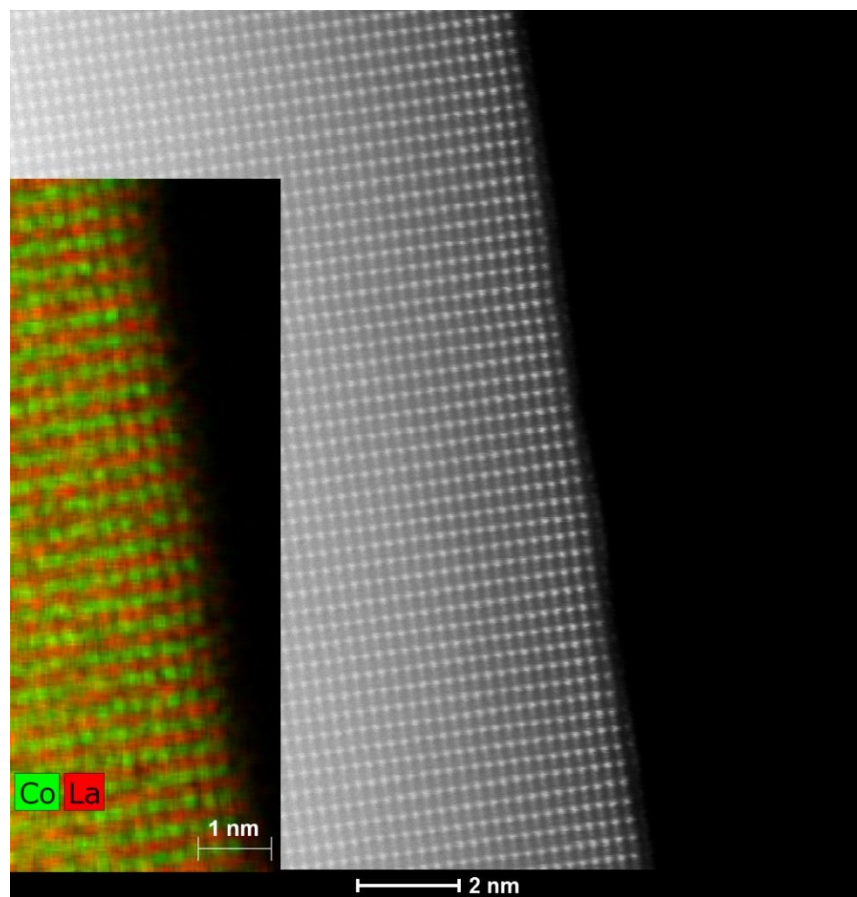
Figure S5: HAADF-STEM image and atomic resolution EDX compositional Co (green) and La (red) map of the {110}$_p$ surface of LaCoO$_3$ nanoparticles in the <1$\bar{1}$0>$_p$ orientation. The terminating layer of the perovskite structure is the (LaCoO) layer.
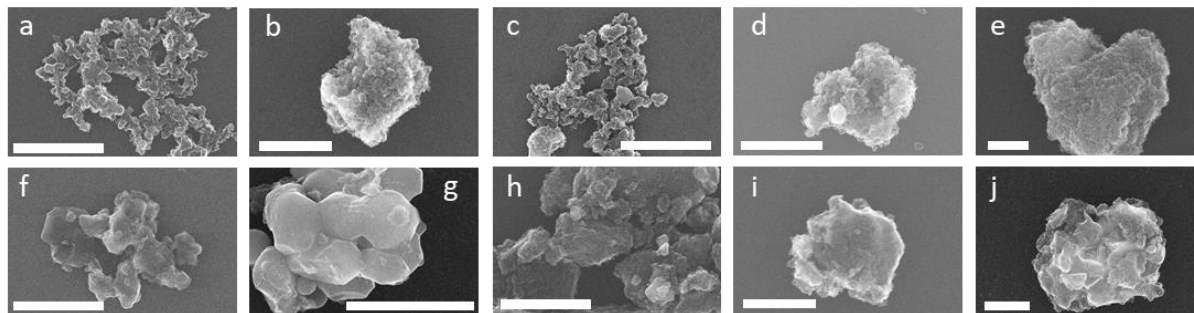
Figure S6: SEM images of the neat carbons and the LSCO perovskite/carbon composites. **a**) VC, **b**) LCO/VC, **c**) LSCO64/VC, **d**) LSCO46/VC, **e**) SCO/VC, (f) NC, (g) LCO/NC, (h) LSCO64/NC, (i) LSCO46/NC, (j) SCO/NC. VC is composed of small ~100 nm sphere shaped particles while NC are larger 300-500 nm flakes. Both carbons appear to form similar conformal coatings around the LSCO particles. The scale bar in all images is 1 μm
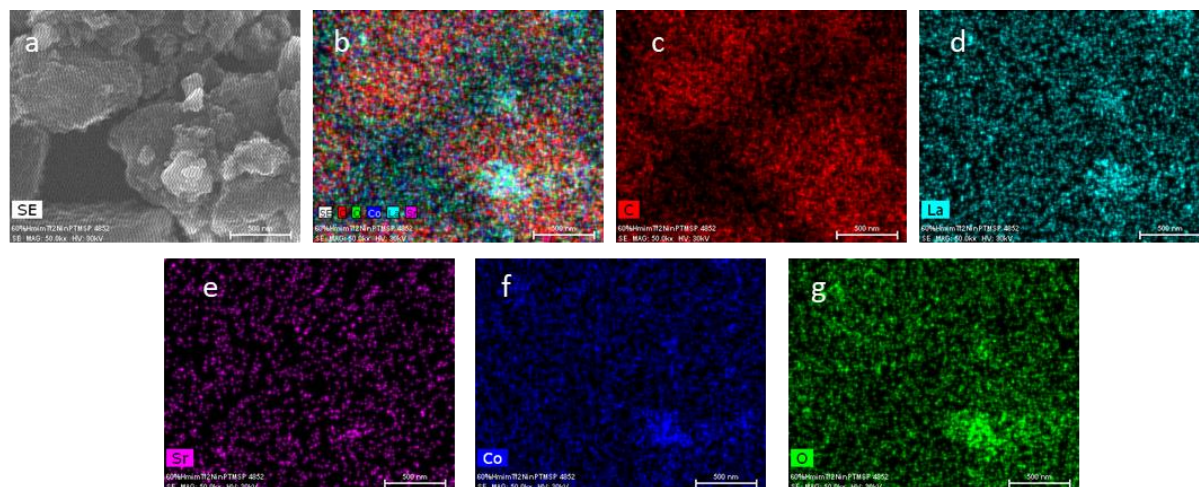
Figure S7: EDS chemical mapping of LSCO64/NC. **a**) Secondary electron SEM image, **b**) EDS chemical map overlay of the different elements, **c**) carbon map shown in red, **d**) lanthanum in turquoise, **e**) strontium in purple, **f**) cobalt in blue, and **g**) oxygen in green.

15
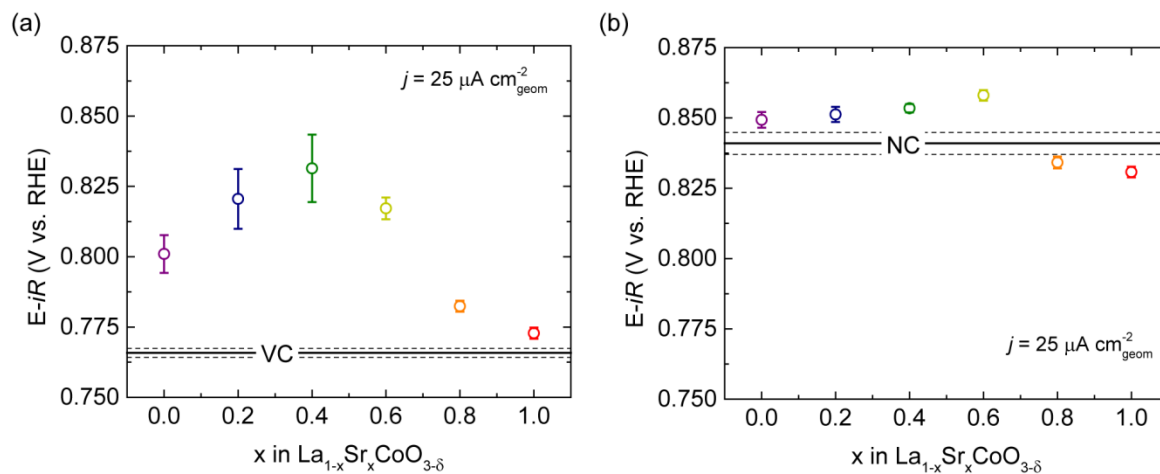
Figure S8: Oxygen reduction onset potentials in O_2 saturated 0.1M KOH at a scan rate of 5 mV s^{-1} in the negative direction for 30 wt% LSCO supported on **a**) Vulcan carbon and **b**) Nitrogen doped mesoporous carbon. The onset potentials for the isolated carbons are shown as lines on the graph with dotted lines indicating the standard deviation of the potential. The onset potential is defined as 25 µA cm^{-2}_{geom} and the error bars represent standard deviations of 5 separate measurements. It can be seen that the onset potential is strongly correlated to the carbon support, indicative of the role of carbon in the activation of O_2 and production of the hydroperoxide ion HO_2^-.
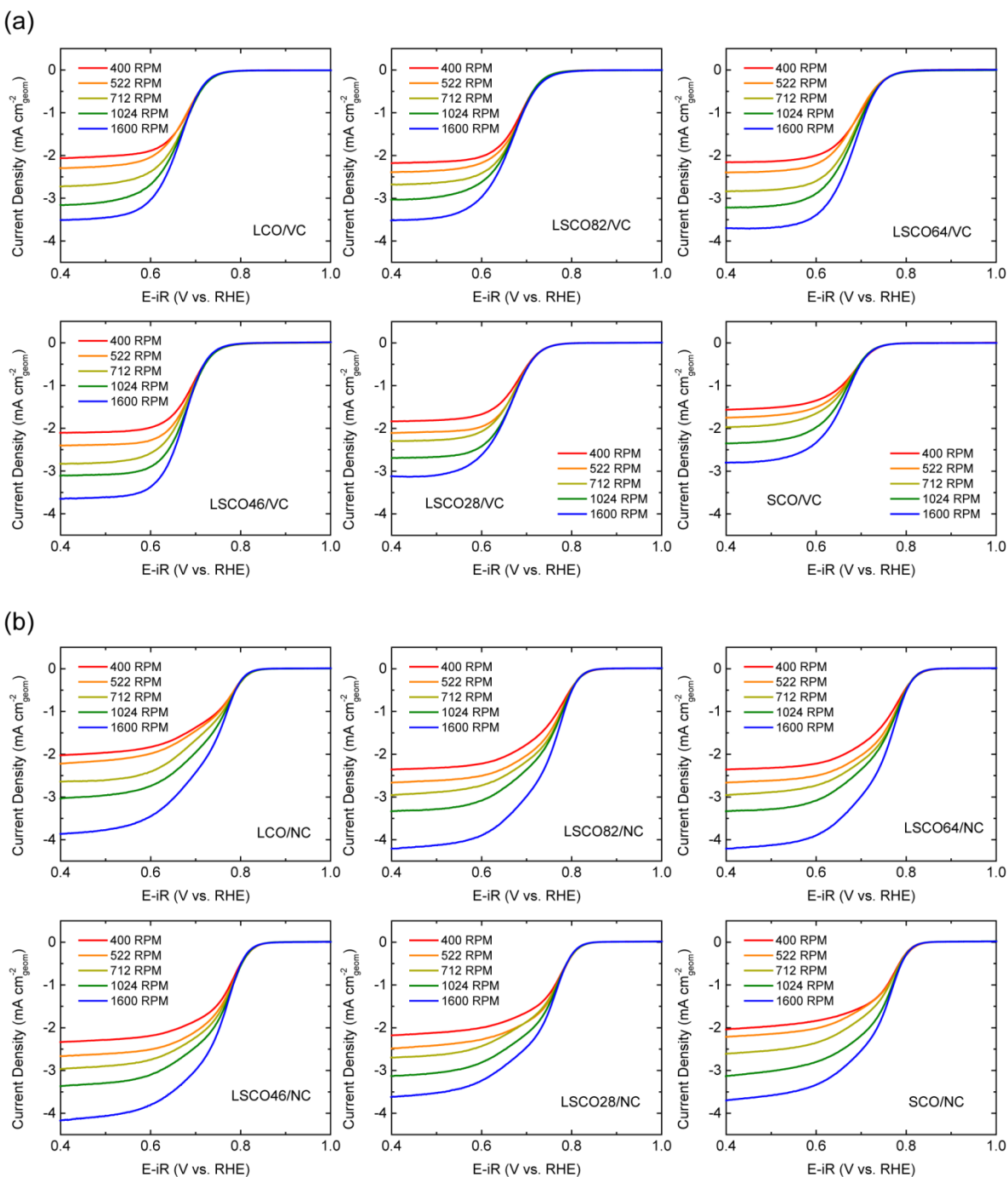
Figure S9: Levich analysis of 30 wt% LSCO perovskite composite electrocatalysts supported on (a) Vulcan carbon and (b) nitrogen-doped mesoporous carbon at a scan rate of 5 mV s^{-1} in the negative potential direction in O_2 saturated 0.1M KOH. Total electrode mass loadings were 51 μg cm$^{-2}_{geom}$. All polarization curves have been *iR* corrected.
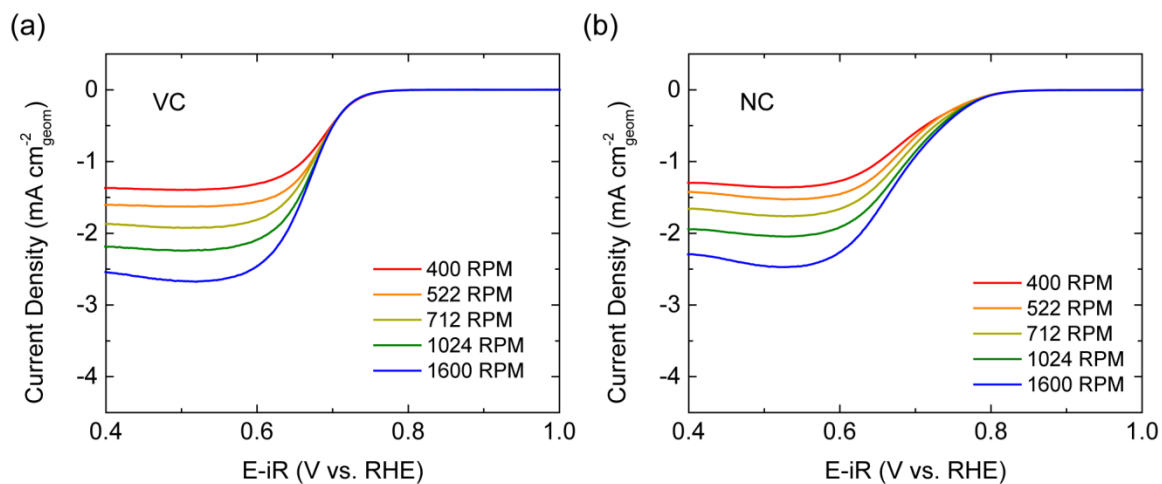
Figure S10. Levich analysis of (**a**) Vulcan carbon and (**b**) nitrogen-doped mesoporous carbon at a scan rate of 5 mV s^{-1} in the negative potential direction in O$_2$ saturated 0.1M KOH. Electrode mass loadings were 35.7 µg cm$^{-2}_{geom}$. All polarization curves have been *iR* corrected.
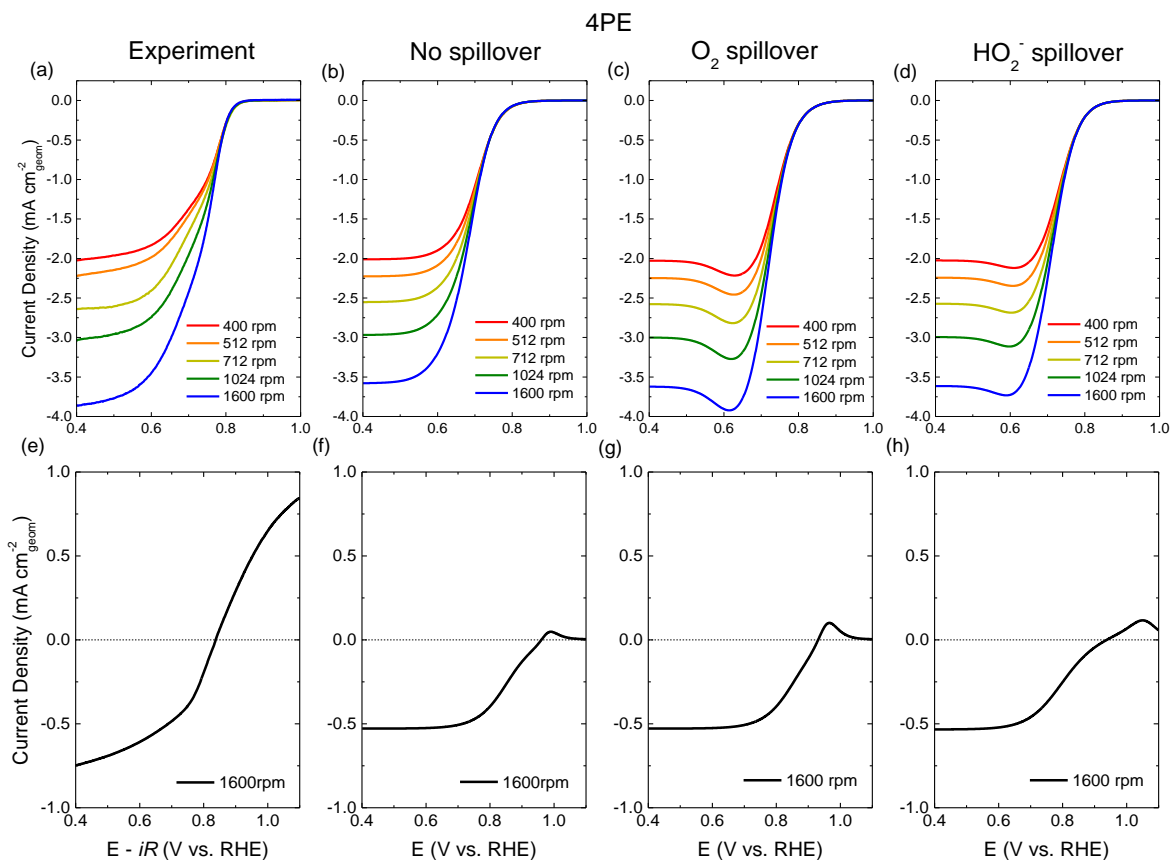
Figure S11. ORR RDE voltammograms (a-d) in O_2 saturated 0.1M KOH. HPRR/HPOR RDE voltammograms (e-h) in Ar-purged 0.1 KOH solution with 1.2mM HO_2^-. 30 wt% LCO/NC composite catalyst was used with total electrode mass loading equal to 51 µg cm^{-2}_{geom}. (**a, e**) experimental results. (**b, f**), (**c, g**), (**d, h**) modeling results for (4PE) reaction mechanism without/with O_2/with HO_2^- spillover respectively.

4PC

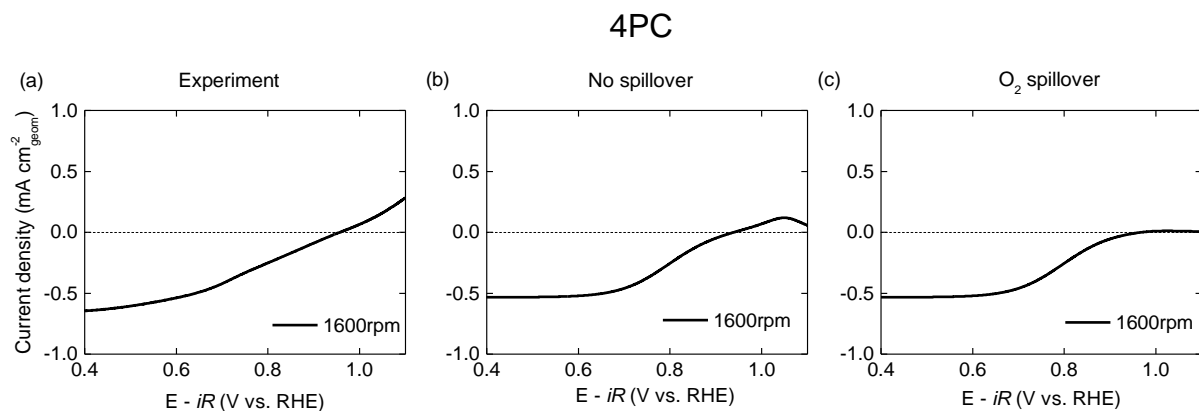**(a)** Experiment   **(b)** No spillover   **(c)** O_2 spillover

Figure S12. HPRR/HPOR RDE voltammograms (**a-c**) in Ar-purged 0.1M KOH with 1.2 mM HO_2^-. 30 wt% LCO/VC composite catalyst was used with total electrode mass loading equal to 51 μg cm^{-2}_{geom}. (**a**) experimental results. (**b, c**) modeling results for (4PC) reaction mechanism without/with O_2^- spillover, respectively.
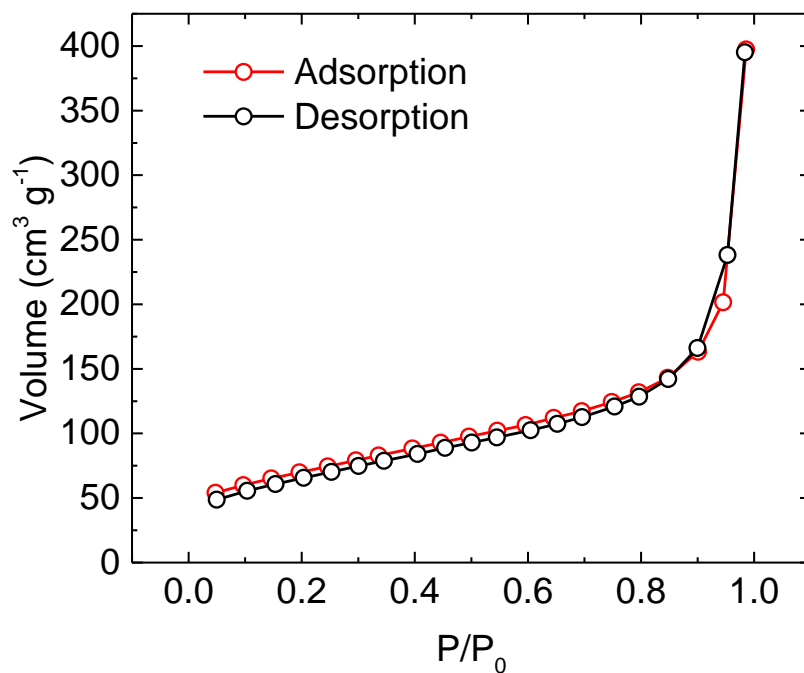
Figure S13. N$_2$ Adsorption/Desorption Isotherm for the Vulcan carbon XC-72 post ball-milling. Brunauer-Emmett-Teller analysis yields a surface area of 235 m^2 g^{-1}.

Supporting References:

1. S. Mickevičius, S. Grebinskij, V. Bondarenka, B. Vengalis, K. Šliužienė, B. A. Orlowski, V. Osinniy and W. Drube, *Journal of Alloys and Compounds*, 2006, **423**, 107–111.
2. K. A. Stoerzinger, W. T. Hong, E. J. Crumlin, H. Bluhm, M. D. Biegalski and Y. Shao-Horn, *J. Phys. Chem. C*, 2014, **118**, 19733–19741.
3. J. Stoch and J. Gablankowska-Kukucz, *Surf. Interface Anal.*, 1991, **17**, 165–167.
4. M. F. Sunding, K. Hadidi, S. Diplas, O. M. Løvvik, T. E. Norby and A. E. Gunnæs, *Journal of Electron Spectroscopy and Related Phenomena*, 2011, **184**, 399–409.
5. J.-C. Dupin, D. Gonbeau, P. Vinatier and A. Levasseur, *Phys. Chem. Chem. Phys.*, 2000, **2**, 1319–1324.
6. V. Young and T. Otagawa, *Applications of Surface Science*, 1985, **20**, 228–248.
7. T. L. Barr, *J. Phys. Chem.*, 1978, **82**, 1801–1810.
8. S. Ponce, M. A. Peña and J. L. G. Fierro, *Applied Catalysis B: Environmental*, 2000, **24**, 193–205.
9. M. a Peña and J. L. Fierro, *Chemical reviews*, 2001, **101**, 1981–2017.
10. R. Schaub, P. Thostrup, N. Lopez, E. Lægsgaard, I. Stensgaard, J. K. Nørskov and F. Besenbacher, *Phys. Rev. Lett.*, 2001, **87**, 266104.
11. O. Bikondoa, C. L. Pang, R. Ithnin, C. A. Muryn, H. Onishi and G. Thornton, *Nat Mater*, 2006, **5**, 189–192.
12. H. P. Boehm, *Discussions of the Faraday Society*, 1971, **52**, 264.
13. I. Morcos and E. Yeager, *Electrochimica Acta*, 1970, **15**, 953–975.
14. T. Poux, A. Bonnefont, G. Kéranguéven, G. A. Tsirlina and E. R. Savinova, *ChemPhysChem*, 2014, **15**, 2108–2120.
15. T. Poux, A. Bonnefont, A. Ryabova, G. Kéranguéven, G. A. Tsirlina and E. R. Savinova, *Phys. Chem. Chem. Phys.*, 2014, **16**, 13595–13600.
16. A. J. Bard and L. R. Faulkner, *Electrochemical Methods: Fundamentals and Applications*, John Wiley & Sons, Inc., New York, 2nd edn., 2001.
17. H. A. Gasteiger and P. N. Ross, *J. Phys. Chem.*, 1996, **100**, 6715–6721.